



STEREO-PIV STUDY OF TURBULENT FLOW DOWNSTREAM OF A BEND IN A ROUND PIPE

Jun Sakakibara*, Rikiya Sonobe*, Hideyuki Goto*,
Hideaki Tezuka**, Hiroyuki Tada**, Kenichi Tezuka**

*Department of Engineering Mechanics and Energy,
University of Tsukuba, Tsukuba, 305-8573, Japan

** Engineering R&D Division, Tokyo Electric Power Company,
Egasaki-Cho 4-1, Tsurumi-Ku, Yokohama-Shi, Kanagawa, 230-8510, Japan

KEYWORDS:

Main subject(s): *Turbulent pipe flow with bend*

Fluid: *Water*

Visualization method(s): *Stereo PIV*

Other keywords: *Proper Orthogonal Decomposition*

ABSTRACT : *We measured three-components of velocity vector distribution in cross sections of a fully developed turbulent pipe flow downstream of a 90-degree bend by means of stereo PIV. Reynolds number was $Re=120,000$, and ratio of inner diameter d of the pipe and radius of the centerline of the bend was 1.5. Proper orthogonal decomposition (POD) was applied to the velocity field in cross-sections. At a streamwise distance $z=2d$ downstream from the bend, the power spectrum of the time-dependent POD coefficient of the 2nd mode shows a dominant peak at $St=0.07$. The power of the 1st and 2nd mode structures identified at $z/d=2$ were switched further downstream, and the structure of 2nd mode at $z/d=2$ tends to be dominant. Reconstruction of the velocity vector field based on the 1st mode at $z/d=2$ with mean velocity vectors gives flow pattern similar to that of swirl switching, while the 2nd mode at $z/d=2$ is responsible to the rotation of the symmetry plane of the twin vortices.*

1 Introduction

Flow in a pipe with a 90° bend has been paid particular attention because of its importance in engineering applications and interesting feature of spatially evolving flow structure upstream and downstream the bend (Berger and Talbot, 1983; Ito, 1987). While the flow at small Dean number with laminar inlet condition consists of a pair of steady counter-rotating vortices, the flow at larger Dean number with turbulence exhibited unsteady and anti-symmetric behavior of the secondary flow. Tunstall & Harvey (1968) found a secondary circulation which does not conform to the twin-circulatory flow as observed in a laminar small Dean number flow. The secondary flow is dominated by a single circulation about the axis in either a clockwise or an anticlockwise sense, between which it switches abruptly at a low frequency, so called ‘swirl switching’. Brucker (1998) performed PIV measurement of the cross sections of the pipe downstream the bend, and confirmed the switching of swirl direction with a low frequency. Rutten et al. (2005) computed the flow in the bend with upstream and downstream straight sections by large eddy simulation (LES). They determined the power spectra of the overall forces onto the pipe walls. At the largest Reynolds number they performed the spectra

exhibited an oscillation at a frequency much lower than that commonly observed at vortex shedding from separation at the inner side of the bends. The associated flow pattern was similar to the swirl switching phenomenon.

Objective of the present study is to capture the dominant structure in the flow field by use of proper orthogonal decomposition (POD). Stereo-PIV was used to measure the three-component planar velocity field in cross-sections of the pipe.

2 Method

2.1 Experimental apparatus and condition

The experiment was conducted with a closed loop circuit of round pipe outlined in Fig.1. The working fluid was tap water purified by cartridge filters with 25 μm and 50 μm pore size. Diameter of the pipe was $d=50$ mm all over the circuit. Centrifugal pump (MDH-401SE5-D, Iwaki) is followed by a perforated plate and a flow straightener consisting of an aluminum honey comb, and the flow development section of $80d$ in length before a 90 degrees pipe bend. Ratio of the radius of the center line of the bend to the pipe diameter was 1.5. The bend was followed by straight test section having $160d$ in length. The pipe bend, which was milled from a block of Plexiglas by CNC, has a thickness of 5 mm. Both of the flow development section and the test section are placed horizontally and are made by Plexiglas pipe in a thickness of 2.5 mm. Rest of the pipe system was constructed from PVC water pipe except upstream and downstream side of the pump, where Tetron blade hose with the length of 4 m each was connected in between the pump and PVC pipe in order to reduce the propagation of the vibration from the pump to the circuit. The test sections were surrounded by Plexiglas rectangular container filled with water, i.e water jacket, to minimize the distortion of the image observed across the round surface of the pipe. The pump was controlled by variable-frequency drive (L100-022LFR, Hitachi) and the flow rate was monitored by an electromagnetic flow meter (AXF050G, Yokogawa). Bulk Reynolds number ν was set to $\text{Re} = U_b d / \nu = 1.2 \times 10^5$, here U_b and ν represent bulk velocity and kinematic viscosity, respectively.

We employed a rectangular Cartesian coordinate system (x, y, z), where y is normal to a symmetry plane of the bend, z is parallel to the centerline of the straight pipe downstream the bend, and x is normal to both y and z . The origin of the coordinate system was set at the center of the pipe in a cross-section at the end of the bend. The mean velocities for the x, y and z components are U, V and W , respectively, and u, v and w are the velocity fluctuations of each component.

2.2 Measurement system

We employed a stereoscopic PIV that is capable of resolving time-dependent, three-component velocity. The water was seeded homogeneously with polyamide-12 tracer particles (Daicel-Degussa, DAIAMID: 1.02 ~ 1.03 sp gr, 40- μm average diameter). A laser light sheet of 2 mm in thickness was produced by a Nd-YLF laser (DM-10-527, 10 mJ/pulse at 1kHz, Photonics Industries) through a cylindrical lens to illuminate a plane normal to z -direction. Twin high-speed C-MOS cameras (Fastcam 1024-PCI, 1024x1024 pixels, 1000 fps in maximum, Photron) were positioned to view the tracer particles at the same region of interest covering whole cross-section of the pipe. In order to measure the velocity field in the cross-section of the pipe as much as close to the bend, one of the camera placed

upstream side captured images reflected by a vertical flat mirror, as shown in Fig.2, while the other camera viewed without mirror. By this configuration the minimum streamwise distance from the end of the bend to the measurement plane was approximately $2d$. The angle between the axes of observation by two cameras was set to about 90° , and their lenses were mounted to satisfy the Scheimpflug condition. A triangle prism consists of Plexiglass water container was placed closely to the water jacket to minimize astigmatism aberration of the image due to inclined incidence of the optical axis to the test section. Whole set of laser with power supply, cameras and optics were fixed on a custom-made linear translation stage, shown in Fig.3, having a stroke of approximately 9000 mm in a direction parallel to the test section.

Stereo-PIV requires camera calibration procedure which makes warping functions between image coordinate and physical coordinate based on images of ‘calibration plate’, on which many markers are printed at known positions. It is better to perform *in situ* calibration, i.e. calibration plate was placed at a plane where the light sheet comes to illuminate, in order to compensate the distortion of image due to the round surface of the pipe. In the present study, however, it is difficult to insert calibration plate into the middle of a long test section without opening the pipe system. Instead of in site calibration, we performed off site calibration out of the test section, referred to as ‘calibration station’. The calibration station consisted of calibration plate with a three orthogonal linear stages and short section of Plexiglas pipe with water jacket, whose design of cross-section facing to the cameras was identical to that of the test section, as shown in Fig.1. A side of the pipe not facing the cameras was opened to allow insertion of the calibration plate into the inside of the pipe. The calibration station was placed further away from the end of the test section but its centerline of the pipe was precisely aligned to that of the test section. Whole set of the cameras and laser was translated to the calibration station until the laser light sheet came to coincide with a surface of calibration plate. After capturing sets of images of calibration plate, the translation stage with cameras and laser was translated back to the position where the PIV image was to be recorded. This configuration allowed capturing the calibration plate image which is closely identical to that placed *in situ*.

Since our camera could typically capture 768 successive time-dependent pairs of images for each camera at a single recording, the same number of instantaneous three-component velocity maps with data rate of 62.5 Hz were obtained. In order to get well converged statistics and temporal power spectrum, we repeated recording 30 times for a fixed condition and location of measurement. Thus the total of 11520 instantaneous velocity map was obtained at a single location. PIV interrogation was performed at equally-spaced Cartesian grid points with interval of $\Delta x=2\text{mm}$ and $\Delta y=2\text{ mm}$ in x and y direction respectively.

The time interval separating the two PIV single exposures was set to 0.1ms, and the mean displacement of the particle was approximately 3.5 pixels. Since the error in measuring the displacement of the tracers was within 0.1 pixels, the error of the instantaneous velocity was estimated to be 2.9 % of the mean velocity. The spatial resolution of the velocity measurement was limited by the size of the interrogation spot. Consider a sinusoidal velocity with spatial wavelength L and size N of the interrogation spot of the PIV. Gain G of the measured velocity compared with the true velocity was derived Hart(2000),

$$G = |L \sin(\pi N / L) / (\pi N)|$$

In the present measurements, the dimensions of the interrogation spot were approximately $N_z=2.7\text{ mm}$ (28 pixels) in the x direction and $N_y=1.7\text{ mm}$ (28 pixels) in y direction. Thus, the wavelength at which the gain dropped 50% ($G=0.5$) was computed as 4.5 mm and 2.8 mm in the z and y directions, respectively. This wavelength was approximately 6%-9% of the pipe diameter, and 2 order magnitude

larger than the estimated Kolmogorov length scale ($\eta \sim 0.04$ mm) of the present flow. Obviously, the results shown in this paper will be focused on large-scale structures without resolving small dissipative eddies.

2.3 Proper Orthogonal Decomposition

Proper orthogonal decomposition (POD) was applied to the 2D3C velocity field in the flow downstream the bend in order to capture the coherent structures. POD is a method to expand random velocity vector function u into optimum basis functions φ . Let $u_i(x, y)$ be an i -th component of velocity vector on a two-dimensional finite domain D , and to be expanded in the form:

$$u_i(x, y; t) = \sum_{n=1}^N a_n(t) \varphi_i^{(n)}(x, y). \quad (1)$$

The statement of optimality is that we want to find a basis function φ to maximize the mean-square correlation with u :

$$\max \frac{\overline{\int_D u_i(x, y; t) \hat{\varphi}_i(x, y) dx dy}}{\left(\overline{\int_D \varphi_i(x, y) \hat{\varphi}_i(x, y) dx dy} \right)^{1/2}}, \quad (2)$$

where over bar denotes time average. The summation convention is implied for repeated indices in this paper unless otherwise stated. It can be shown by the methods of calculus of variation that the φ is a solution of

$$\int_D R_{ij}(x, y; x', y') \hat{\varphi}_j(x', y') dx' dy' = \lambda \varphi_i(x, y) \quad (3)$$

where $R_{ij} = \langle u_i(x, y) u_j(x', y') \rangle$ is the two-point correlation function, and $\langle \rangle$ denotes ensemble average.

This was discretized to lead algebraic eigenvalue problem

$$\mathbf{A} \varphi = \lambda \varphi \quad (4)$$

where \mathbf{A} is a $3N \times 3N$ matrix with N being a number of grid point in domain D which covers whole cross section of the pipe. The time-dependent POD coefficient, $a_j(t)$, was then computed by projecting velocity vector field onto the basis

$$a_n(t) = \int_D u_i(x, y; t) \varphi_i^{(n)}(x, y) dx dy. \quad (5)$$

Throughout the paper, the POD mode number n was arranged in a descending order of the eigenvalues.

3 Result and discussion

Fig.4 shows power spectrum of POD coefficient for first three eigenvalue. The spectrum was averaged over 30 independent spectrum computed from 768 successive velocity data by FFT. Reduced frequency is defined by $St = fD/U_b$. At $z/d=2$ a peak near $St=0.07$ is observed in the power spectrum of 2nd mode, while the 1st mode is smaller in magnitude at such a low frequency. Further downstream at $z/d=10$, the 1st mode becomes dominant in the low frequency range, while the spectrum of the 2nd mode is quite similar in shape to the one of the 1st mode at $z/d=2$, specifically a gradual bump near the $St=0.4$. This fact suggest that the eigenvalue of the 1st mode at $z/d=2$ became lower than that of 2nd mode on the way to $z/d=10$, and the order of the eigenvalue of these two modes, or structures, has been switched. Such a switching of the mode is also evident in $z/d=15$ where the 2nd and 3rd POD mode is similar in

shape to that of 3rd and 2nd mode at $z/d=10$. Thus we summarize that the 1st mode at $z/d=2$, hereafter referred to as ‘initial 1st mode’, decays its eigenvalue to the 2nd one at $z/d=10$, and then decays further to 3rd one at $z/d=15$. While the initial 1st mode decays as travel downstream, the 2nd and the 3rd mode at $z/d=2$, similarly referred to as ‘initial 2nd mode’ and ‘initial 3rd mode’, respectively glow up to 1st mode at $z/d=10$ and to the 2nd mode at $z/d=15$.

Downstream evolution of the three eigenfunctions is presented in Fig.5. While the single swirling flow pattern is observed in the 1st mode at $z/d=2$, 2nd and 3rd mode exhibited counter-rotating vortices at the same streamwise location. The initial 1st mode structure, which turn into the 2nd and 3rd mode at $z/d=10$ and 15, respectively, continued to show similar pattern as traveling downstream, although the center of the swirl was slightly shifted outer side of the bend. The initial 2nd mode, which turn into the 1st mode downstream, tends to dominate only a single swirl pattern centered in the left side of the figure at $z/d=10$ and further downstream.

The counter rotating Dean vortices is not necessary to be shown in the eigenfunctions, because the Dean vortices are already characterized in the mean velocity field and the patterns of the eigenfunction is a fluctuating part added to the mean velocity. Thus the physical appearance of the Dean vortices might not be obvious in the single eigenfunction. The role of each eigenfunction in the appearance of the instantaneous structures might be more visible in velocity vector field reconstructed by mean velocity vectors added to the eigenfunction scaled by arbitrary POD coefficient, formed by

$$\tilde{u}_i(x, y) = A\lambda^{(n)/2}\varphi_i^{(n)}(x, y) + \bar{u}_i(x, y)$$

where A is an arbitrary constant value. The square-root of the eigenvalue, $\lambda^{(n)/2}$, is identical to the root-mean square value of $a_n(t)$ that represents a characteristic amplitude of time-dependent fluctuating POD coefficient. Figure 6 shows streamwise evolution of the velocity field reconstructed by eigenfunctions for initial 2nd mode. Typical Dean vortices formed by a pair of counter-rotating vortices are visualized in a range of $z/d=2-15$. Variation of A demonstrates the rotation of the symmetry line of vortices around the center of the pipe. The amplitude of the rotation is approximately 20 degrees at $z/d=2$ and doubled at $z/d=10$ and 15. Rutten et al.(2005) presented a temporal variation of the angular position of the stagnation point computed from the spatial-low pass filtered velocity. Its peak-to-peak amplitude of the stagnation position was within $\pm 40^\circ$. Assuming the standard deviation is a half of this value, it is comparable to the present result at $z/d=2$.

Velocity vector field reconstructed by the initial 1st mode is shown in Fig.7. The flow pattern at $z/d=2$ exhibited counter-rotating vortices similar to that appeared in Fig.6, but the vortices are displaced in y -direction with a change of A rather than just rotating around the center of the pipe shown in Fig.6. At $z/d=10$ and 15, the displacement of the vortices is significant and one of the vortices occupies much more area than others. Such behavior is qualitatively similar to the phenomenon of swirl switching observed by Tunstall et al. (1968).

4 Conclusion

The stereo-PIV has been used to measure the cross-sectional distribution of three-component velocity vector in a turbulent pipe flow downstream the 90 degrees bend. Proper orthogonal decomposition was applied to decompose instantaneous flow field into a set of eigenfunctions in order to capture the unsteady nature of the energetic structures. The initial 1st mode which gives flow pattern similar to that of swirl switching has the largest contribution to the turbulent kinetic energy at $z/d=2$, but its

contribution decays as traveling downstream. Instead of the initial 1st mode, initial 2nd mode which is responsible to the rotation of the symmetry plane of the twin vortices makes more contribution further downstream.

References

- Tunstall, M.J., Harvey, J.K., "On the effect of a sharp bend in a fully developed turbulent pipe-flow," *J.Fluid Mech.* 34, 595-608 (1968).
- Rutten, F., Schroder, W., Meinke, M., "Large-eddy simulation of low frequency oscillations of the Dean vortices in turbulent pipe bend flows," *Phys. Fluids* 17, 035107 (2005).
- Rutten, F., Meinke, M., Schroder, W., "Large-eddy simulations of 90° pipe bend flows," *J. Turbulence*, 2, 003 (2001).
- Brucker, Ch., "Time-recording DPIV-study of the swirl switching effect in a 90° bend flow," *Proc. 8th Int. Symp. Flow Vis.*, Sorrento, Italy, 1998.
- Berger, S.A., Talbot, L., "Flow in curved pipes," *Ann. Rev. Fluid Mech.* 15, 461-512 (1983).
- H. Ito, "Flow in curved pipes," *JSME Int. J.* 30, 543-552 (1987).
- Hart, D. P., "PIV error correction," *Exp. Fluids* 29, 13 (2000).

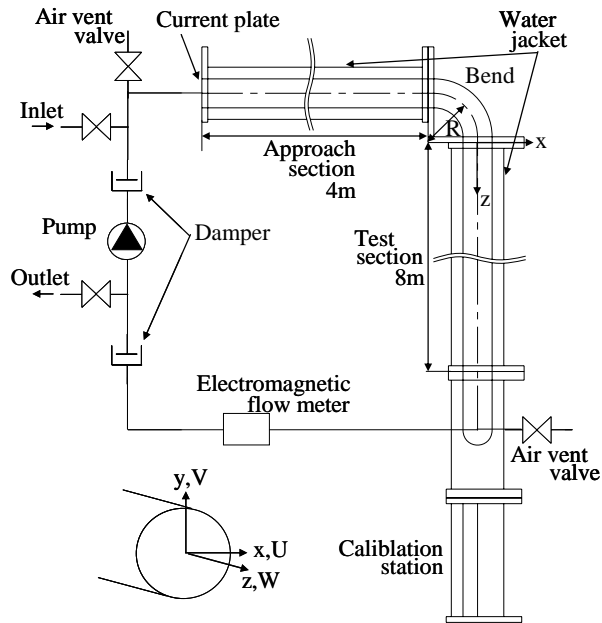


Fig.1 Top view of test section and flow circuit.

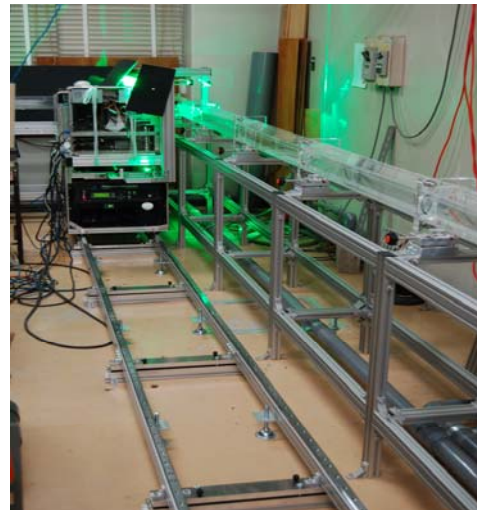


Fig.3 Translation stage carrying laser and cameras along the test section.

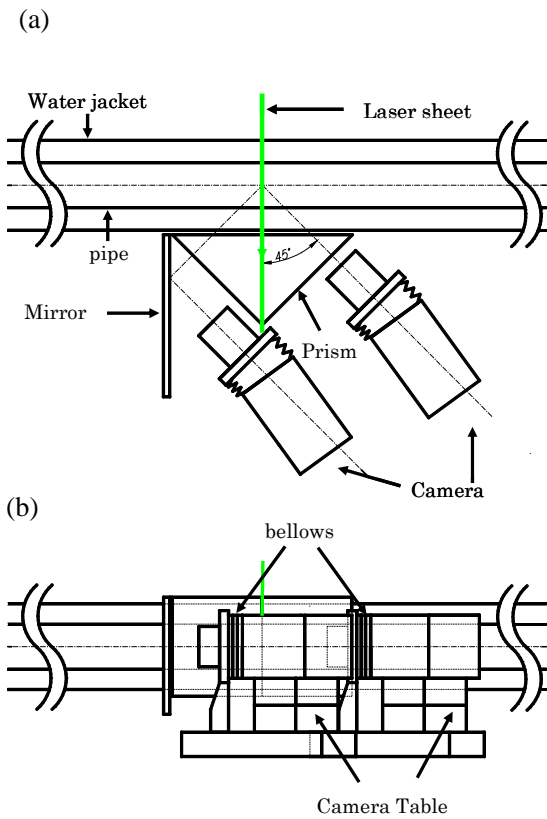


Fig.2 Arrangement of cameras and optics against the test section. (a) top view, (b) side view.

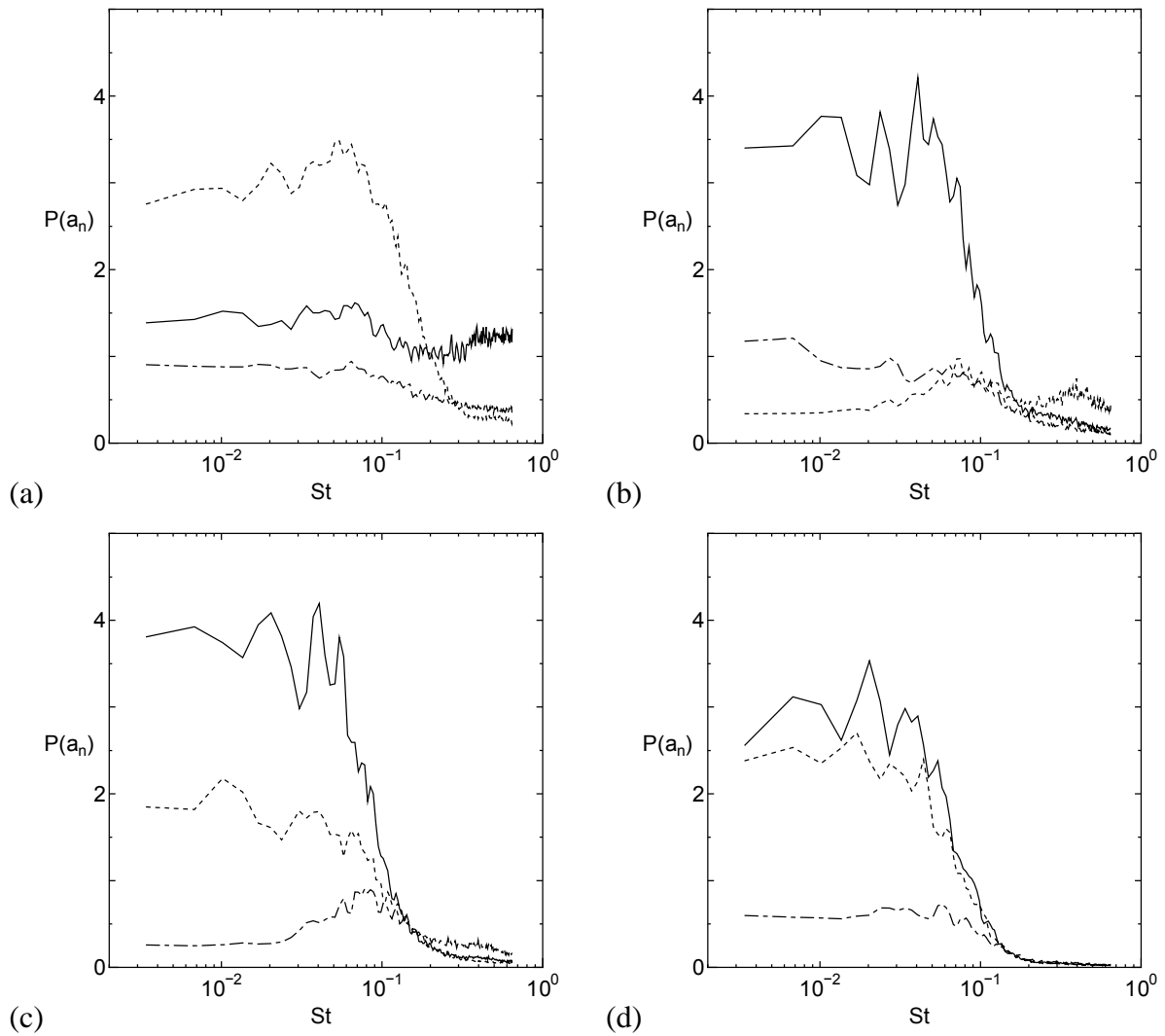


Fig.4 Streamwise evolution of power spectrum of POD coefficient. (a) $z/d=2$, (b) $z/d=10$, (c) $z/d=15$, (d) $z/d=25$. solid: 1st mode, dashed: 2nd mode, dotted line: 3rd mode.

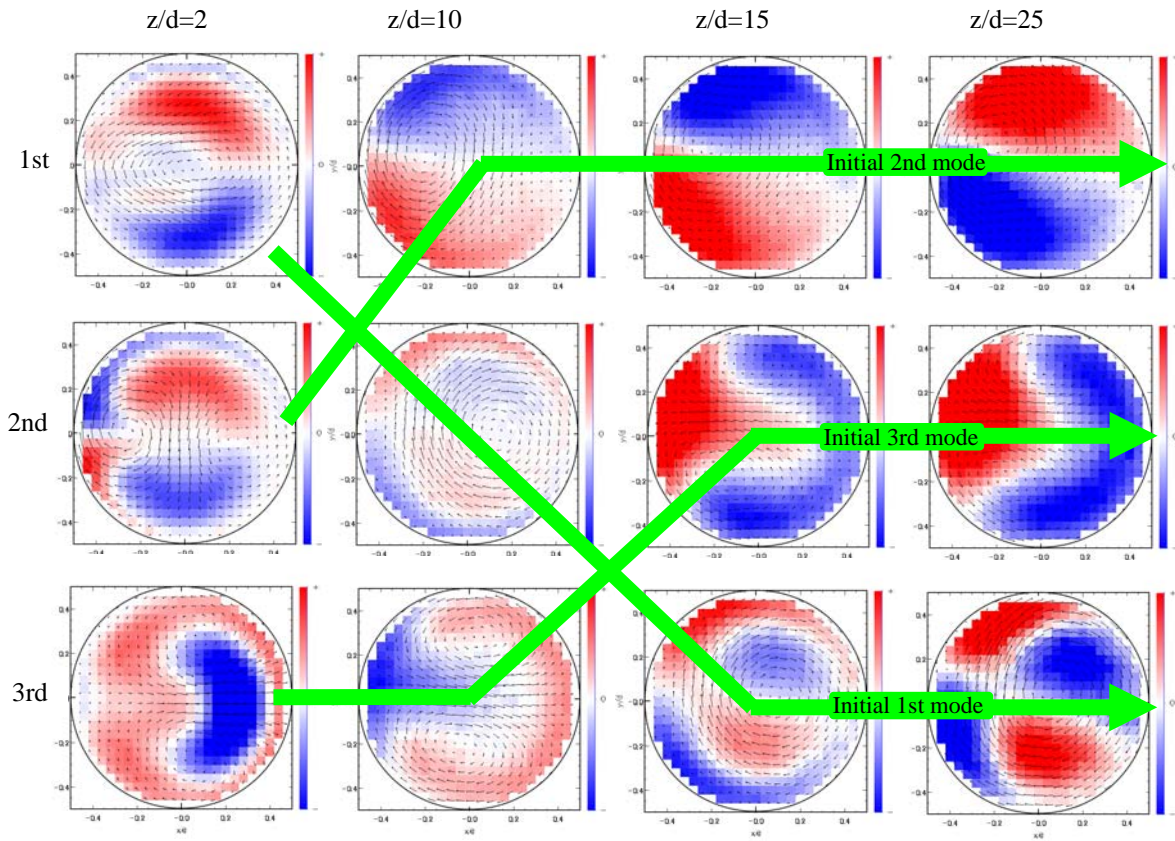


Fig5 Streamwise evolution of eigenfunction. Color indicated w -component of the function.

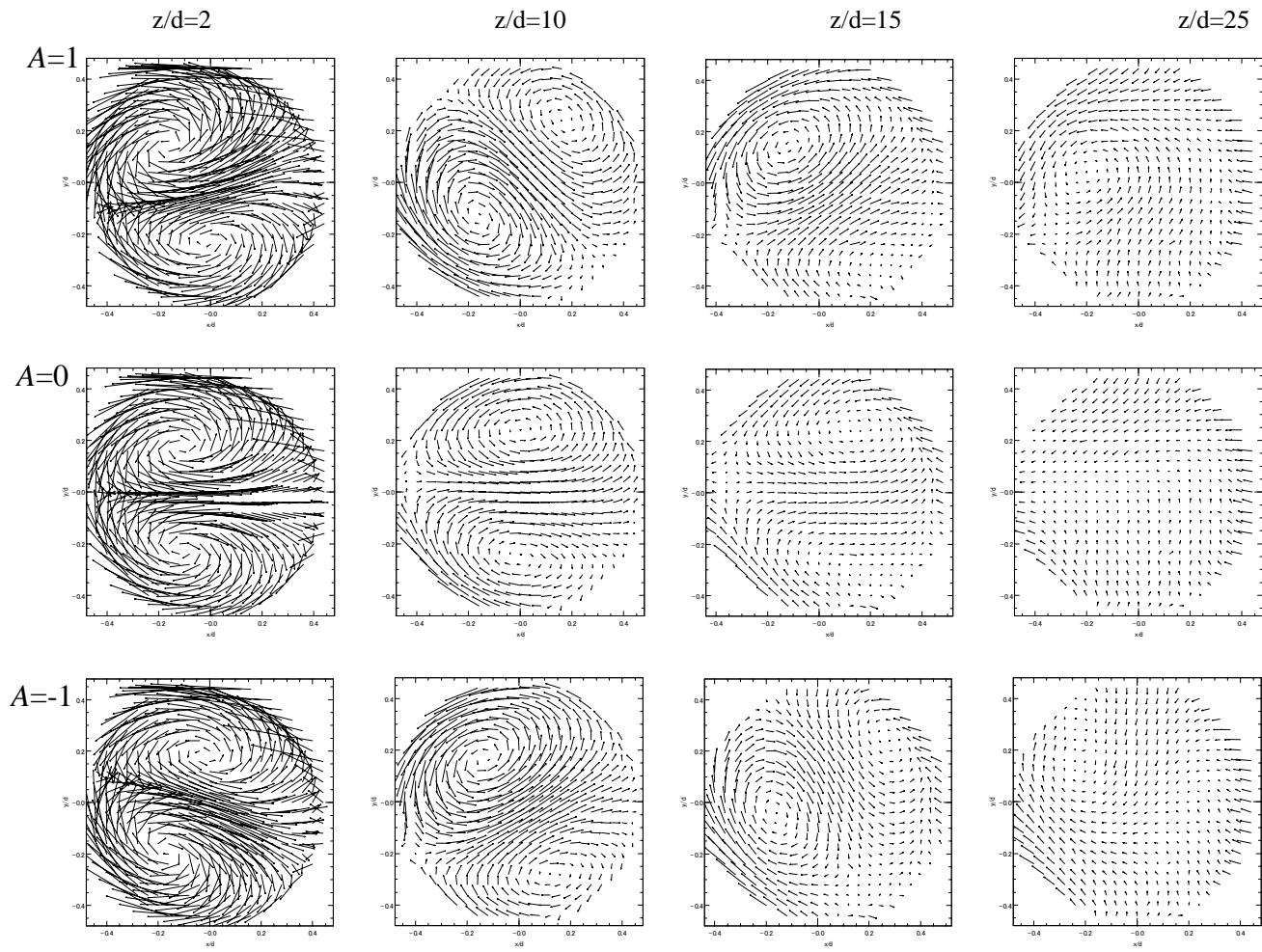


Fig.6 Velocity vectors reconstructed by initial 2nd eigenfunction and mean velocity vectors.

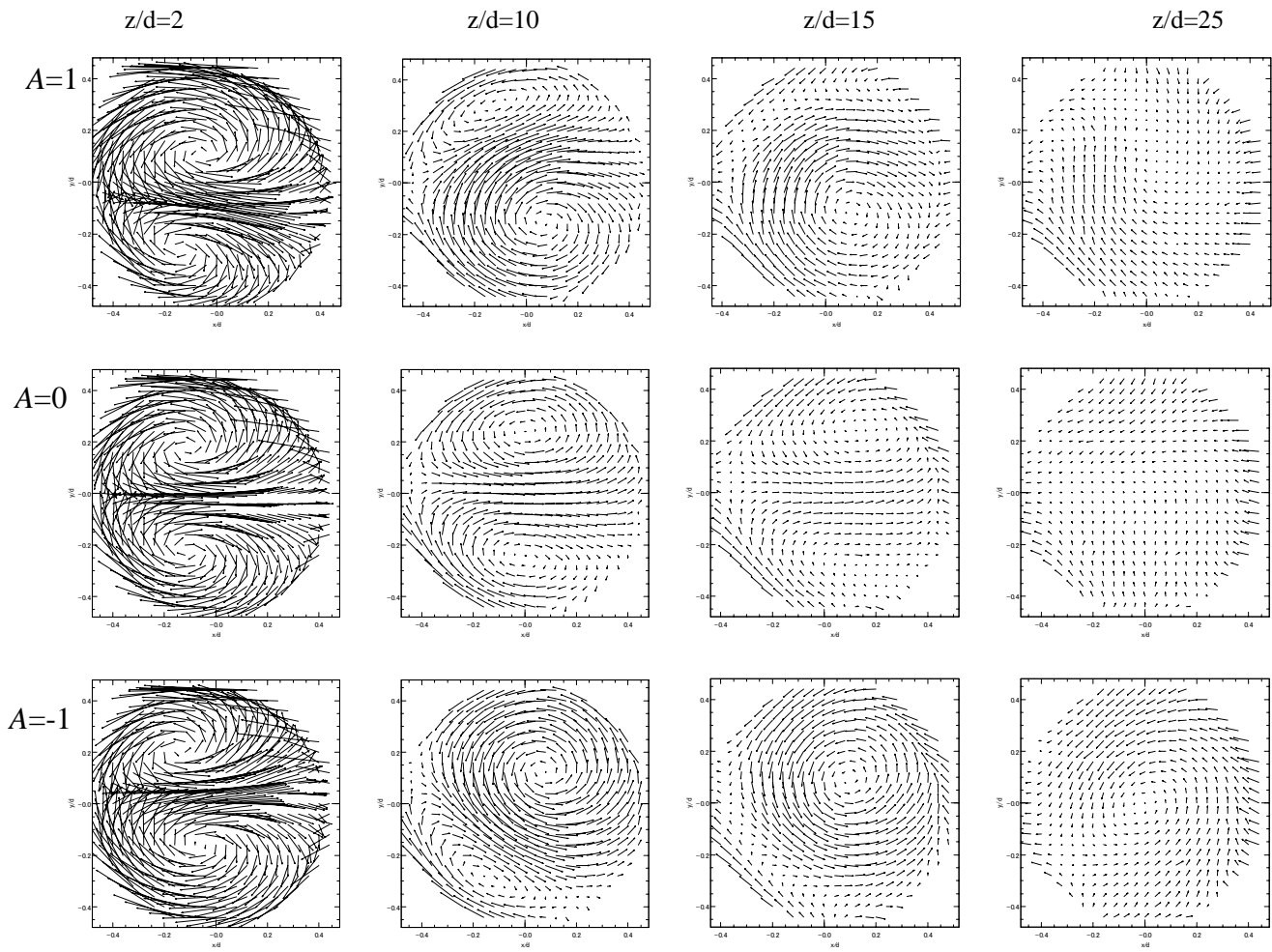


Fig.7 Velocity vectors reconstructed by initial 1st eigenfunction and mean velocity vectors.